

Accepted Manuscript

Failure modes in high strength and stiffness to weight scaffolds produced by Selective Laser Melting

Timothy B. Sercombe, Xiaoxue Xu, V.J. Challis, Richard Green, Sheng Yue, Ziyu Zhang, Peter D. Lee

PII: S0261-3069(14)00851-6

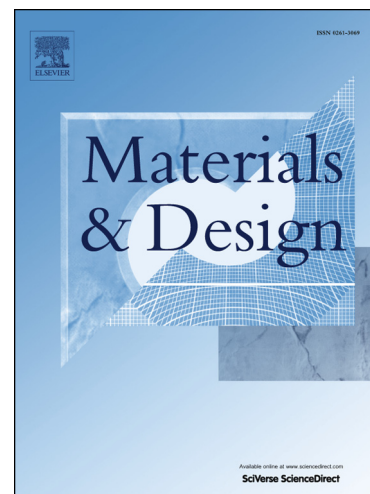
DOI: <http://dx.doi.org/10.1016/j.matdes.2014.10.063>

Reference: JMAD 6922

To appear in: *Materials and Design*

Received Date: 24 June 2014

Accepted Date: 23 October 2014



Please cite this article as: Sercombe, T.B., Xu, X., Challis, V.J., Green, R., Yue, S., Zhang, Z., Lee, P.D., Failure modes in high strength and stiffness to weight scaffolds produced by Selective Laser Melting, *Materials and Design* (2014), doi: <http://dx.doi.org/10.1016/j.matdes.2014.10.063>

This is a PDF file of an unedited manuscript that has been accepted for publication. As a service to our customers we are providing this early version of the manuscript. The manuscript will undergo copyediting, typesetting, and review of the resulting proof before it is published in its final form. Please note that during the production process errors may be discovered which could affect the content, and all legal disclaimers that apply to the journal pertain.

Failure modes in high strength and stiffness to weight scaffolds produced by Selective Laser Melting

Timothy B. Sercombe^{1,*}, Xiaoxue Xu^{1,1}, V.J. Challis², Richard Green³, Sheng Yue³, Ziyu Zhang⁴ and Peter D. Lee³

1. School of Mechanical and Chemical Engineering, The University of Western Australia, Perth, WA 6009 Australia

2. School of Mathematics & Physics, The University of Queensland, St Lucia, QLD 4072, Australia

3. School of Materials, The University of Manchester, Manchester, M13 9PL, UK

4. Department of Materials, Prince Consort Road, Imperial College London, London SW7 2BP, UK

* Corresponding author. Phone: +61 8 6488 3124. Email: tim.sercombe@uwa.edu.au

Abstract

The production of porous scaffold structures using additive manufacturing is becoming widespread, however a detailed understanding of the scaffold failure mechanisms is lacking. In this research, Selective Laser Melting (SLM) is used to produce Ti-6Al-4V scaffold structures consisting of a regular array of unit cells previously designed using topology optimisation. Interrupted compression testing and subsequent X-Ray Micro Tomography (XMT) characterisation is used to study the deformation and failure of the scaffolds for a range of solid fractions. Further, the XMT data of the unloaded scaffolds is used to generate meshes for finite element analysis which allowed direct comparison of desired and as built behaviour. Likely failure sites predicted from the finite element analysis compare favourably with the experimentally observed ones. Failure is initiated in areas that exhibit the greatest tensile stress, while the onset of the commonly observed layered failure occurs afterwards. The XMT of the unloaded scaffolds also highlights the inaccuracies in the SLM build process, which contributes to stress concentrations in the horizontal arms within the scaffolds. The results indicate that although the strength of the topology optimised structures is very high, further refinement in both the unit cell design and build quality would further increase the strength.

Keywords

Selective Laser Melting, X-ray computed tomography, titanium alloys, porous material, Finite-element analysis

¹ Present Address: Department of Chemistry and Biomolecular Sciences, Macquarie University, Sydney, NSW 2109, Australia

1. Introduction

The use of porous materials for regenerative medicine is attracting increasing interest due to the ability to control the stiffness [1, 2] of the device as well as promote the in growth of bone [3]. In load bearing applications, polymers and ceramics do not possess the requisite mechanical strength and toughness to survive the *in vivo* loading and therefore metals and their alloys have become the material of choice [4].

The relatively low modulus of titanium, along with its excellent corrosion resistance and very high specific strength, has resulted in it being widely favoured for bone replacement applications [4, 5]. Even so, Ti has a modulus which is at least an order of magnitude larger than bone. Mismatch of moduli between the biomaterial and surrounding bone can cause stress shielding in the bone, which eventually leads to bone resorption, and has been identified as a major causal factor of implant loosening [3, 6]. The modulus of a material can be decreased by introducing porosity, which, provided it is interconnected, can have the additional desired effect of promoting bone in-growth [7-9], along with easy diffusion of nutrients to and waste from the implant [10, 11].

There are a number of methods to produce porous titanium components (see [12-14] for recent reviews). Of these methods, only additive manufacturing ("3D printing") techniques enables the fabrication of anatomically-shaped scaffolds with complex internal architectures, allowing precise control of the porosity (including pore size, shape and interconnectivity) and therefore stiffness.

The mechanical strength of porous materials is determined largely by the characteristics of the pores – namely their size, volume fraction and shape [15], as these dictate the size of the load bearing struts. There have been a number of methods used to predict the mechanical behaviour of porous solids. Gibson and Ashby [16] have developed a micromechanical model to predict the strength of foams based on the physical characteristics such as relative density, the nature of the porosity (ie open or closed) and the material properties of the metal. Predictions using continuum micromechanics were subsequently developed [17] to overcome some of the limitations of the Gibson-Ashby models (namely assumptions of uniform porosity, idealised smooth struts and the absence of any axial or shear displacement of the foam edges during loading). A third approach has been to use finite element modelling (FEM) of the three dimensional (3D) structure and has been used to predict the compressive behaviour of bone [18], titanium [19-21], aluminium [22-26] and bioactive glasses [27]. This modelling work usually has been accompanied by X-Ray Micro Tomography (XMT), which can be used to quantify the 3D microstructure, generate the required FEM meshes and directly study the deformation behaviour [21, 28-30] and flow properties [31] and bone in growth [32] into porous solids. This provides insights into the failure mechanisms, especially the prediction of the most vulnerable localised regions.

Recently [2] we have shown the advantage of combining topology optimisation and Selective Laser Melting (SLM) to produce structures with exceptionally high strength and stiffness to weight. However, we do not understand the deformation or failure mechanisms of these structures, which is hindering our ability to improve the design further. In this work, we have studied the failure of topology optimised structures [1, 33] using interrupted compression testing and XMT characterisation, allowing the direct comparison of the desired properties and failure mechanisms to those actually achieved.

2. Experimental Details

2.1 Part Manufacture

In this work, scaffolds were created from a unit cell that was designed using topology optimisation [1, 33] at three different nominal solid fractions, 7%, 10% and 15%. The base unit cell of the 10% solid fraction is shown in Figure 1. These unit cells have exceptionally high strength and stiffness to weight ratio [2].

Structures consisting of 3x3x3 unit cells, 3.333mm in size (overall size 10x10x10mm³), were manufactured using Selective Laser Melting (SLM) on a Realizer SLM100 machine (Borchen, Germany). The Ti-6Al-4V powder that was used was obtained from TLS Technik, Germany. A scanning electron image (Zeiss 1555 VP-FESEM, Jena, Germany) of the powder is shown in Figure 2 and the important characteristics of the powder are summarised in Table 1. The composition was measured using inductively coupled plasma atomic emission spectroscopy (ICP-AES) by Spectrometer Services (Melbourne, Australia), the particle size using a Malvern Microsizer Plus (Worcestershire, UK) and the flow and apparent density according to Metal Powder Industries Federation Standard 03 and 04 [34], respectively. The theoretical density of the alloy was taken to be 4.43g/cm³.

The SLM processing parameters used are summarised in Table 2. Each slice was divided into regions that were “on solid” (that is contained at least one layer of solid beneath them) or “on powder” (which contained only powder below, such as would occur on the overhangs of downward facing surfaces). Determination of the “on powder” and “on solid” areas was performed using the Realizer software. The control of the laser speed is achieved through the independent setting of a point distance (d) and exposure time at each point (t) and therefore the overall laser speed is d/t . In all cases the parts were built on a commercially pure Ti substrate plate, using an Ar atmosphere that contained <1000ppm of oxygen. The layer thickness, laser scan spacing and laser offset were kept constant at 50, 100 and 60µm, respectively. The direction of the laser was rotated 90° between layers and was always parallel to the edge of the scaffold structures. After building, the parts were removed from the substrate, the support structure was removed and the parts cleaned by glass bead blasting and then compressed air. The dimensions of the scaffold and weight were then measured to an accuracy of 10µm and 1mg respectively in order to calculate the density and therefore solid fraction. A comparison between the nominal solid fraction with that of the CAD model and the as-built scaffold structures is shown in Table 3.

2.2 X-Ray Micro Tomography

In situ X-Ray Micro Tomography (XMT) was used in conjunction with interrupted compression testing to study the compressive deformation of the scaffolds. The sample was loaded into a Deben rig (St Edmunds, UK), with a maximum load rating of 10kN and compressed at a constant strain rate of 0.05mm/min. The loading direction was parallel to the build direction of the sample. Prior to, and periodically during compression, the sample was held at a constant strain, and a 360° tomographic scan performed. The XMT was performed using a Nikon Metris 225 (Nikon Metrology, UK) at 130kV and 300µA with a voxel size of 24.5 µm. Projections (2000, 250ms exposure time) were collected on a 2k x 2k charge-coupled device detector. XMT images were then reconstructed from these

projections using a cone beam back-projection algorithm. A schematic of the experimental set up is shown in Figure 3.

2.3 FEA Analysis

Volumes of individual unit cells with different solid fractions (7%, 10% and 15%) from the XMT scans were segmented and meshed in a commercial FEM meshing package, ScanIP (Simpleware Ltd., UK). The FEM meshes were then imported into the FEM analysis package Abaqus/CAE (Dassault Systemes Simulia Corp., USA). Figure 4 shows the schematic of the 3D FEA model and the boundary conditions applied in the simulation, along with the material bulk properties. The modulus of the bulk material was determined using separately produced, machined rectangular samples ($48 \times 11 \times 5 \text{ mm}^3$) built parallel to the horizontal axis of the machine, using an impulse excitation technique on a Grindosonic™ instrument (Heverlee, Belgium). These bars were subsequently machined into tensile samples (gauge length $6 \times 4 \times 15 \text{ mm}^3$), and tested on an Instron 5982 (Norwood, MA, USA), using a 10mm extensometer and at a cross head speed of 1mm/min. The testing direction was normal to the build direction. The top surface node set was assigned a constant load along z-direction and the bottom surface node was restricted from moving in the z-direction. Note that due to the different strengths of the various solid fractions, the force was scaled with the solid fraction, i.e. a load ratio of 2:5:10 was used for the 7%, 10% and 15% solid fractions respectively. In addition to the single unit cells, FEA analysis on the ideal unit cell (model) and a $3 \times 3 \times 3$ volume of the actual 10% solid fraction structure were performed.

3. Results.

The structure of the central cell from the 10% solid fraction scaffold is compared to the computer model from which it was built in Figure 5. It is clear that the geometrical reproduction of the model is not perfect. In particular, there are localised increases in the size (“Z-growth”) of the vertical members (see Figure 5(c)) resulting in high surface roughness of the downwards facing surfaces. In contrast, upwards facing surfaces are relatively smooth and well defined. For the horizontal members, shown in Figure 5(d), the thickness is much less than the model and also contains significant variability and roughness. Nonetheless, as shown in Figure 5 (e) and (f), both the horizontal and vertical arms are solid and contain only a low level of porosity. FEA analysis of the ideal unit cell, Figure 6, reveals that under uniaxial compression, the horizontal arms carry tensile loading, while the vertical arms are loaded in compression.

The mechanical behaviour of the scaffolds at the various solid fractions is shown in Figure 7 together with the points at which the compression test was interrupted for scanning. The general shape of the stress strain curve is similar to that of a conventional bulk material.

Progressive deformation of the 10% solid fraction scaffold at points (a) – (d) in Figure 7 is shown in Figure 8. This Figure shows that gradual deformation of the vertical sections occurs prior to shear failure at an angle of 45° to the applied load. Figure 8(e) is a 3D rendering of the final failed structure. Similar deformation characteristics were observed in all solid fraction samples.

The initial failure site for the three solid fractions was identified in the reconstructed XMT data from the point just beyond the peak load (shown in Figure 7). These failure sites are indicated on the isolated individual unit cell in which they occurred in Figure 9 alongside the stress distribution as predicted by the FEA. For all solid fractions, the first failure occurred in the horizontal arms and the

exact failure location aligned with regions of high tensile stress due to build variations as predicted by the FEA.

The locations where the scaffold collapses can be seen in Figure 10. This is for the central layer of the 10% solid fraction structure at stress 'c' in Figure 7, well beyond the peak load. It is apparent that failure progressed via multiple fracturing of the horizontal arms (Figure 10(a)), with the vertically aligned members remaining intact, Figure 10(c). The site of the fractures is also indicated on the FEA results in Figure 10(b). Similar to what was shown in Figure 9, there is a very close correlation between the high stress areas and location of the failures. The failure of the horizontal arms prior to the vertical arms occurred on all layers of the scaffold and for all three solid fractions.

4. Discussion

The geometric freedom afforded by advanced manufacturing technologies such as SLM facilitates the production of previously unachievable geometries. However, the accuracy of the reproduction of the structure is limited by the fact that the process is powder based and also by the local instabilities in the melt pool that can form during the scanning of the laser across the powder bed. At high laser energies the cylindrical melt pool can become unstable due to rapid convective motion known as thermo-capillary or Marangoni flow [35-38]. This instability causes the melt pool to break up into large non-continuous droplets, an effect usually called "balling". If the energy density is too low however, insufficient melting creates a smaller melt pool and if the length to diameter ratio of this melt pool becomes larger than π , small balls form, commonly thought to occur as a result of Rayleigh instability [35, 39, 40]. Between these two extremes, smooth regular scan tracks form. However even these can form irregularities due to localised changes in the thermal conditions [41]. Of particular concern are overhangs or unsupported horizontal surfaces. In these regions, the laser scans across powder that does not have any solid material below. During SLM, heat conduction through the underlying solid causes rapid cooling of the laser scanned material and therefore higher laser energies are required to compensate [35]. Since loose powder has significantly lower thermal conductivity than solid metal, a lower energy is required to fully melt the powder. The use of the same energy will cause superheating of the melt pool, diffusion of the heat into the underlying powder, and melting of powder from beyond the layer being scanned. Consequently, the scanning strategy employed divided each slice in to areas which have solid beneath ("on solid") and areas which have powder beneath ("on powder"). A different set of parameters were used for each area (Table 2). Despite this lowered energy, it is apparent that on downwards facing surfaces (see Figure 5(b)) the laser energy penetrates beyond the layer being scanned and is sufficient to melt, or partially melt, the powder, causing surface roughness and growth in the z-direction. However this penetration is not consistent, which may be a result of localised variability in the powder packing and hence thermal conductivity.

Unsupported horizontal arms can also be problematic to build via SLM. Residual stresses and aforementioned variability in powder packing can result in the formation of unstable melt tracks, which causes the significant surface roughness (Figure 5(c)). Figure 5 also shows that the horizontal arms are thinner than the model, possibly as a result of contraction of the liquid pool as it solidifies, which would act to increase the stress levels in these sections.

Despite the inaccuracies in the build, this unit cell possesses exceptional strength and stiffness to weight [2]. However, mechanism(s) by which these structures fail has not been investigated, which

prevents further refinement of the design. Failure of random porous structures, such as foams, tends to occur via collapse of the entire horizontal layer containing the weakest strut soon after yielding [22, 42, 43]. As a result of this failure mechanism, a rapid drop in the strength often occurs soon after yielding. This is due to the concentration of the stress in the material surrounding the failure site causing subsequent localised collapse of the structure. Similar behaviour has been reported in Selective Laser or Electron Beam Melted scaffold structures [9, 44-47], with a sudden drop in the stress occurring immediately after yielding and where localised failure along an angle of 45° to the applied load is often observed [9, 46, 47]. However, it is apparent from Figure 7, that these structures exhibit very different failure behaviour and behave much more like a bulk material – that is beyond yielding, the load carrying capacity of the structure continues to increase. Therefore it appears that a different failure mechanism is in operation.

For all solid fractions studied, failure first occurred in the horizontally aligned struts, Figure 9(a)-(c). These arms carry tensile loading (Figure 6). However, the reduced cross sectional area and significant surface roughness causes the peak stress to be approximately twice that predicted in the ideal unit cell, Figure 9 (d)-(f). Hence it is quite clear that the initial failure not only occurs in the struts that are loaded in tension, but is also located at the regions of high stress concentration due to build variations.

Subsequent to the first failure, continued loading results in progressive fracture of these tension loaded, horizontal struts, Figure 10(a), while the vertically aligned members, which are mostly in compression, remain intact, Figure 10(c). Similar to the initial failure, all the failure sites of the struts occurred at the location of high tensile stress as predicted in the FEA, Figure 10(b). Both the site of first failure and also the way in which the failure propagates did not change with the solid fraction of the structure. In all cases, the horizontal arms fail first, with continued load carrying ability being maintained by the vertical members. Final collapse of the structure occurs as a result of the fracturing/collapse of the vertical arms, which occurs at 45° to the stress direction, Figure 8(d) and (e). Once the horizontal strut arms have fractured, the scaffold structure becomes similar to an octahedral structure, which is known to fail in a localised shear band in both static [47] and fatigue loading [48]. Hence it is apparent that these structures are failing in a way that is very different from the “floor-by-floor” mechanism often observed in porous foams. The result of this is that the initial failure of the scaffold does not cause a large drop in the load carrying capacity of the structure once the yield point is exceeded, which increases the damage tolerance of the design.

5. Conclusions

In this work, we have coupled *in situ* compression testing XMT with FEA to investigate the failure mechanisms of high strength and stiffness to weight scaffold structures, over a range of solid fractions. From this work, we have made the following conclusions:

- It is apparent that the failure of these structures first occurs in the struts that carry the tensile load. Further, failure occurred at the sites that FEA predicted to have high localised stress due to poor build quality. Therefore, by improving the build quality (to minimise the high surface roughness), it may be possible to improve the load carrying capacity of these high strength scaffolds even further. This highlights the feedback/optimisation loop that XMT facilitates, especially when coupled to *in-situ* loading capabilities. The scale and

complexity of these structures means that both optical and electron microscopy are not effective characterisation techniques.

- By combining XMT and FEA, the failure site(s) of the scaffolds can be predicted prior to physical testing and therefore can be used as an important tool in the evaluation of new scaffold designs.
- The failure mode was very different to the classical floor-by-floor mechanism of traditional foam materials and, as a result, significant load carrying capacity was maintained even after the onset of strut failure. Only once all the horizontal arms had failed, was a more traditional failure mode observed, with a shear band forming at 45°.

Acknowledgements

This work was made possible by the facilities and support provided by the Manchester X-ray Imaging Facility and the Research Complex at Harwell, funded in part by the EPSRC (EP/I02249X/1) and the Australian Research Council's Discovery Projects funding scheme (project number DP110101653).

References

1. Challis VJ, Roberts AP, Grotowski JF, Zhang L-C, Sercombe TB. Prototypes for Bone Implant Scaffolds Designed via Topology Optimization and Manufactured by Solid Freeform Fabrication. *Advanced Engineering Materials*. 2010;12:1106-10.
2. Challis VJ, Xu X, Zhang LC, Roberts AP, Grotowski JF, Sercombe TB. High specific strength and stiffness structures produced using selective laser melting. *Materials & Design*. 2014;63:783-8.
3. Robertson, D.M., L. St. Pierre, and R. Chahal, Preliminary observations of bone ingrowth into porous materials. *Journal of Biomedical Materials Research*, 1976. 10(3): p. 335-344.
4. Niinomi, M., Recent metallic materials for biomedical applications. *Metallurgical and Materials Transactions A*, 2002. 33(3): p. 477-486.
5. Wang, K., The use of titanium for medical applications in the USA. *Int. Symp. Metallurgy & Tech. Ti Alloys*, 1996. 213(1-2): p. 134-137.
6. Head, W.C., D.J. Baulk, and R.H. Emersom, Titanium as the material of choice for cementless femoral components in total hip arthroplasty. *Clinical Orthopaedics and Related Research*, 1995. 311: p. 85.
7. Hulbert, S.F., S.J. Morrison, and J.J. Klawitter, Tissue reaction to three ceramics of porous and non-porous structures. *Journal of Biomedical Materials Research*, 1972. 6(5): p. 347-374.
8. Holy, C.E., M.S. Shoichet, and J.E. Davies, Engineering three-dimensional bone tissue in vitro using biodegradable scaffolds: Investigating initial cell-seeding density and culture period. *Journal of Biomedical Materials Research*, 2000. 51(3): p. 376-382.
9. Yang L, Harrysson O, West H, Cormier D. Compressive properties of Ti-6Al-4V auxetic mesh structures made by electron beam melting. *Acta Materialia*. 2012;60:3370-9.
10. Yue S, Lee PD, Poologasundarampillai G, Jones JR. Evaluation of 3-D bioactive glass scaffolds dissolution in a perfusion flow system with X-ray microtomography. *Acta Biomaterialia*. 2011;7:2637-43.
11. Murphy, C.M. and F.J. O'Brien, Understanding the effect of mean pore size on cell activity in collagen-glycosaminoglycan scaffolds. *Cell Adhesion & Migration*, 2010. 4(3): p. 377-381.
12. Singh R, Lee PD, Dashwood RJ, Lindley TC. Titanium foams for biomedical applications: a review. *Materials Technology*. 2010;25:127-36.
13. Dunand, D.C., Processing of Titanium Foams. *Advanced Engineering Materials*, 2004. 6(6): p. 369-376.
14. Ryan, G., A. Pandit, and D.P. Apatsidis, Fabrication methods of porous metals for use in orthopaedic applications. *Biomaterials*, 2006. 27(13): p. 2651-2670.
15. Davies, G.J. and S. Zhen, Metallic foams: their production, properties and applications. *Journal of Materials Science*, 1983. 18(7): p. 1899-1911.
16. Gibson, L.J. and M.F. Ashby, *Cellular Solids: Structure and Properties*. 1999: Cambridge University Press.
17. Zaoui, A., Continuum micromechanics: Survey. *Journal of Engineering Mechanics*, 2002. 128(8): p. 808-816.
18. Crawford, R.P., C.E. Cann, and T.M. Keaveny, Finite element models predict in vitro vertebral body compressive strength better than quantitative computed tomography. *Bone*, 2003. 33(4): p. 744-750.
19. Shen, H. and L.C. Brinson, Finite element modeling of porous titanium. *International Journal of Solids and Structures*, 2007. 44(1): p. 320-335.
20. Thelen, S., F. Barthelat, and L.C. Brinson, Mechanics considerations for microporous titanium as an orthopedic implant material. *Journal of Biomedical Materials Research - Part A*, 2004. 69(4): p. 601-610.
21. Singh R, Lee PD, Lindley TC, Kohlhauser C, Hellmich C, Bram M, Imwinkelried T, Dashwood RJ. Characterization of the deformation behavior of intermediate porosity interconnected Ti foams using micro-computed tomography and direct finite element modeling. *Acta Biomaterialia*. 2010;6:2342-51.
22. Bart-Smith H, Bastawros AF, Mumm DR, Evans AG, Sypeck DJ, Wadley HNG. Compressive deformation and yielding mechanisms in cellular Al alloys determined using X-ray tomography and surface strain mapping. *Acta Materialia*. 1998;46:3583-92.
23. Ohgaki T, Toda H, Kobayashi M, Uesugi K, Kobayashi T, Niinomi M, Akahori T, Makii K, Aruga Y. In-situ High-resolution X-ray CT Observation of Compressive and Damage Behaviour of Aluminium Foams by Local Tomography Technique. *Advanced Engineering Materials*. 2006;8:473-5.

24. Toda H, Ohgaki T, Uesugi K, Kobayashi M, Kuroda N, Kobayashi T, Niinomi M, Akahori T, Makii K, Aruga Y. Quantitative assessment of microstructure and its effects on compression behavior of aluminum foams via high-resolution synchrotron x-ray tomography. *Metallurgical and Materials Transactions A: Physical Metallurgy and Materials Science*. 2006;37:1211-9.
25. Watson IG, Lee PD, Dashwood RJ, Young P. Simulation of the mechanical properties of an aluminum matrix composite using X-ray microtomography. *Metall and Mat Trans A*. 2006;37:551-8.
26. Zhang Q, Lee PD, Singh R, Wu G, Lindley TC. Micro-CT characterization of structural features and deformation behavior of fly ash/aluminum syntactic foam. *Acta Materialia*. 2009;57:3003-11..
27. Jones, J.R., P.D. Lee, and L.L. Hench, Hierarchical porous materials for tissue engineering. *Philosophical Transactions of the Royal Society A: Mathematical, Physical and Engineering Sciences*, 2006. 364(1838): p. 263-281.
28. Hangai Y, Takahashi K, Yamaguchi R, Utsunomiya T, Kitahara S, Kuwazuru O, Yoshikawa N. Nondestructive observation of pore structure deformation behavior of functionally graded aluminum foam by X-ray computed tomography. *Materials Science and Engineering A*. 2012;556:678-84.
29. Michailidis N, Stergioudi F, Omar H, Papadopoulos D, Tsiapas DN. Experimental and FEM analysis of the material response of porous metals imposed to mechanical loading. *Colloids and Surfaces A: Physicochemical and Engineering Aspects*. 2011;382:124-31.
30. Hangai Y, Kato H, Utsunomiyav T, Kitahara S, Kuwazuru O, Yoshikawa N. Effects of porosity and pore structure on compression properties of blowing-agent-free aluminum foams fabricated from aluminum alloy die castings. *Materials Transactions*. 2012;53:1515-20.
31. Zhang Z, Jones D, Yue S, Lee PD, Jones JR, Sutcliffe CJ, Jones E. Hierarchical tailoring of strut architecture to control permeability of additive manufactured titanium implants. *Materials Science and Engineering: C*. 2013;33:4055-62.
32. Zhang Z, Yuan L, Lee PD, Jones E, Jones JR. Modeling of time dependent localized flow shear stress and its impact on cellular growth within additive manufactured titanium implants. *Journal of Biomedical Materials Research Part B: Applied Biomaterials*. 2014;102:1689-99.
33. Challis, V.J., A.P. Roberts, and A.H. Wilkins, Design of three dimensional isotropic microstructures for maximized stiffness and conductivity. *International Journal of Solids and Structures*, 2008. 45(14-15): p. 4130-4146.
34. Standard Test Methods for Metal Powders and Powder Metallurgy Products. 2009, Princeton, New Jersey USA: Metal Powder Industries Federation
35. Yadroitsev, I., P. Bertrand, and I. Smurov, Parametric analysis of the selective laser melting process. *Applied Surface Science*, 2007. 253(19): p. 8064-8069.
36. Gu DD, Meiners W, Wissenbach K, Poprawe R. Laser additive manufacturing of metallic components: materials, processes and mechanisms. *International Materials Reviews*. 2012;57:133-64.
37. Lee, P.D., P.N. Quested, and M. McLean, Modelling of Marangoni effects in electron beam melting. *Phil. Trans. R. Soc. Lond. A*, 1998. 356(1739): p. 1027-1043.
38. Rombouts M, Kruth JP, Froyen L, Mercelis P. Fundamentals of Selective Laser Melting of alloyed steel powders. *CIRP Annals - Manufacturing Technology*. 2006;55:187-92.
39. Gusarov AV, Yadroitsev I, Bertrand P, Smurov I. Heat transfer modelling and stability analysis of selective laser melting. *Applied Surface Science*. 2007;254:975-9.
40. Childs, T.H.C., C. Hauser, and M. Badrossamay, Mapping and Modelling Single Scan Track Formation in Direct Metal Selective Laser Melting. *CIRP Annals - Manufacturing Technology*, 2004. 53(1): p. 191-194.
41. Ciurana, J., L. Hernandez, and J. Delgado, Energy density analysis on single tracks formed by selective laser melting with CoCrMo powder material. *The International Journal of Advanced Manufacturing Technology*, 2013: p. 1-8.
42. Raj, R.E. and B.S.S. Daniel, Structural and compressive property correlation of closed-cell aluminum foam. *Journal of Alloys and Compounds*, 2009. 467(1-2): p. 550-556.
43. Ashby MF. Plastic Deformation of Cellular Materials. In: Editors-in-Chief: KHJB, Robert WC, Merton CF, Bernard I, Edward JK, Subhash M editors. *Encyclopedia of Materials: Science and Technology* (Second Edition). Oxford: Elsevier; 2001. p. 7068-71.
44. Heini, P., C. Körner, and R.F. Singer, Selective Electron Beam Melting of Cellular Titanium: Mechanical Properties. *Advanced Engineering Materials*, 2008. 10(9): p. 882-888.
45. Smith, M., Z. Guan, and W.J. Cantwell, Finite Element Modelling of the Compressive Response of Lattice Structures Manufactured Using the Selective Laser Melting Technique. *International Journal of Mechanical Sciences*, (0).

46. Gorny B, Niendorf T, Lackmann J, Thoene M, Troester T, Maier HJ. In situ characterization of the deformation and failure behavior of non-stochastic porous structures processed by selective laser melting. *Materials Science and Engineering: A*. 2011;528:7962-7.
47. Cheng XY, Li SJ, Murr LE, Zhang ZB, Hao YL, Yang R, Medina F, Wicker RB. Compression deformation behavior of Ti-6Al-4V alloy with cellular structures fabricated by electron beam melting. *Journal of the Mechanical Behavior of Biomedical Materials*. 2012;16:153-62.
48. Li SJ, Murr LE, Cheng XY, Zhang ZB, Hao YL, Yang R, Medina F, Wicker RB. Compression fatigue behavior of Ti-6Al-4V mesh arrays fabricated by electron beam melting. *Acta Materialia*. 2012;60:793-802.

ACCEPTED MANUSCRIPT

Table 1. Selected characteristics of the Ti-6Al-4V powder used in this work.

Table 2. Laser parameters used.

Table 3. . Comparison between the nominal, CAD and actual as fabricated solid fraction for the scaffolds used.

Figure 1. The optimised unit cell at a 10% solid fraction. The samples were built using an array of 3x3x3 cells at 7%, 10% and 15% solid fractions. All struts have the same dimensions

Figure 2. Scanning electron image of the Ti-6Al-4V powder

Figure 3. Schematic of the in situ compression rig. The samples were held at constant strain while the XMT scan was performed.

Figure 4. Bulk properties used in the finite element analysis (a) and the constraints and loading applied (b). The yellow arrows indicate constant load. The orange and blue marks indicate the constraints applied: in the bottom xy-plane there is a symmetry restraint in z translation, x rotation and y rotation. The points where the loading and constraints are applied are equally spaced around the surface of the structure.

Figure 5. Comparison between the CAD file ((a), (b)), actually built unit cell ((c), (d)) and the central slice ((e) and (f)) for the 10% solid fraction scaffold. The side view is shown in (a), (c) and (e), and the top view in (b), (d) and (f). It is apparent comparing (a) and (c) that there is significantly greater surface roughness on the downward facing surfaces, while the horizontal arms (shown in (d)) are smaller than in the model, they are essentially fully dense and integral.

Figure 6. Finite element analysis of the unit cell. It is apparent that the horizontal arms carry the tensile load and the vertical one, compression.

Figure 7. Typical stress strain curves for optimised structures at the solid fractions used as acquired on an Instron material testing machine. The overlaid dots indicate the equivalent position that XMT scans were performed. The numbers indicate the nominal solid fraction of the structure (see Table 3)

Figure 8. Compression of a central slice through the 10% optimised structure at the points (a) to (d) shown in Figure 4. The central plane of unit cells after compression at (d) is rendered in 3D in (e).

Figure 9. Comparison between the (a) – (c) first failure site and (d) – (f) FEA of the starting structure for the three volume fractions used. In all cases, the initial failure site occurred in the horizontal arms and was in an area that the FEA predicts as having high tensile stress. Images are of the top view

Figure 10. XMT and corresponding FEA of the central layer of unit cells for the 10% solid fraction scaffold. This scaffold has been loaded well beyond the peak load (to point C in Figure 6) and exhibits multiple fractures of the horizontal arms (arrowed). The top view is shown in (a) and (b) and the side view in (c) and (d) side view. It is apparent that the failure sites are strongly correlated with the high stress regions in the FEA, which are also indicated with arrowed).

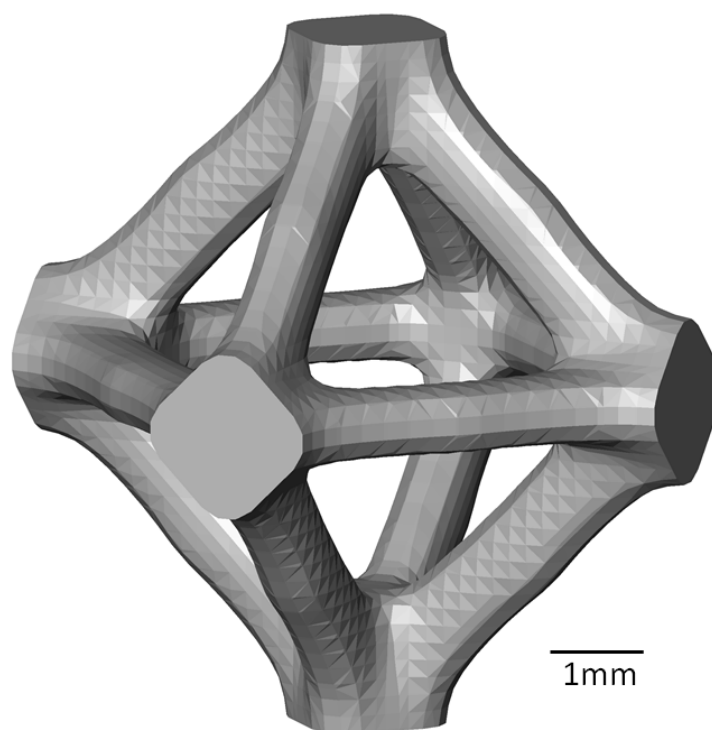


Figure 1

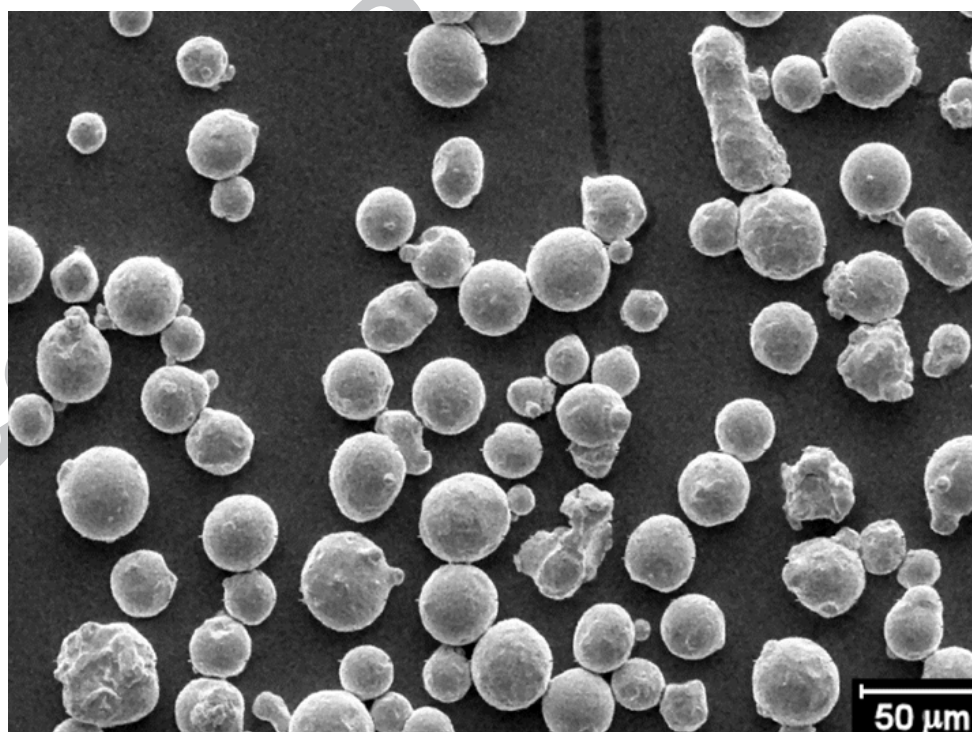


Figure 2

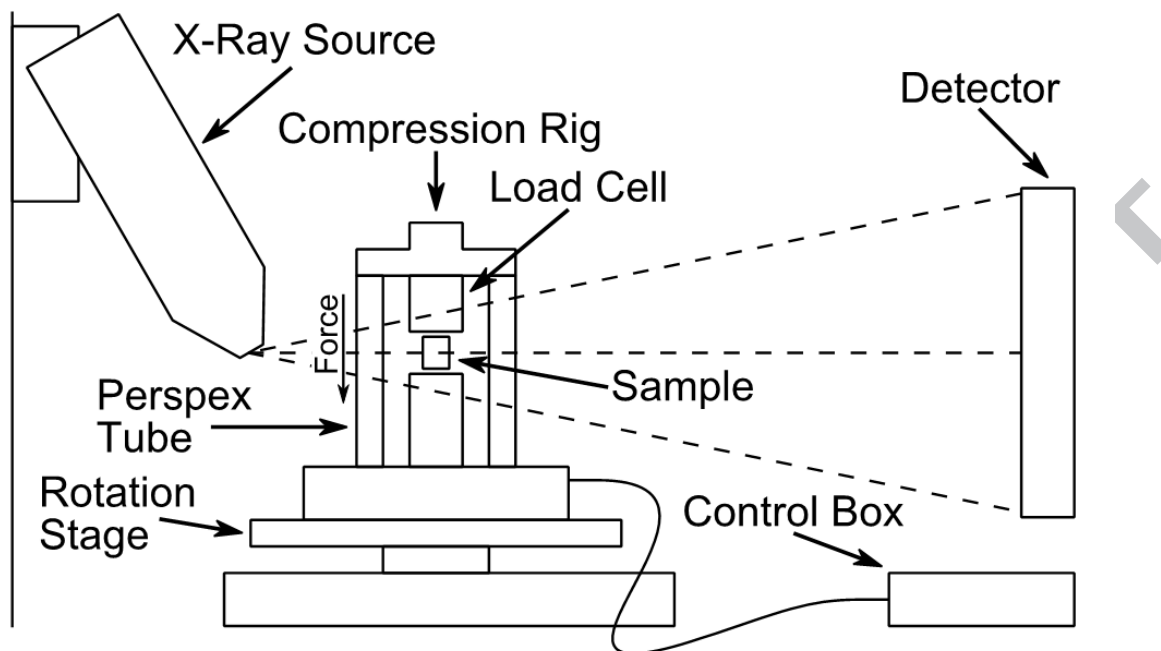
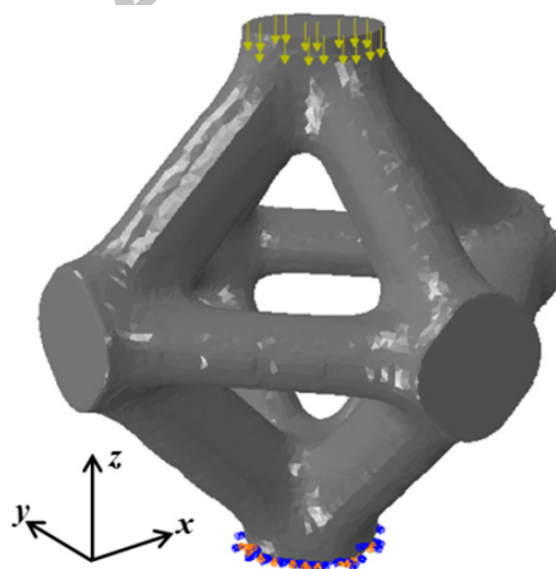


Figure 3

Elastic Modulus	110 <u>GPa</u>
Ultimate Tensile Strength	1150 <u>MPa</u>
Yield Strength	1075 <u>MPa</u>



(a)

(b)

Figure 4

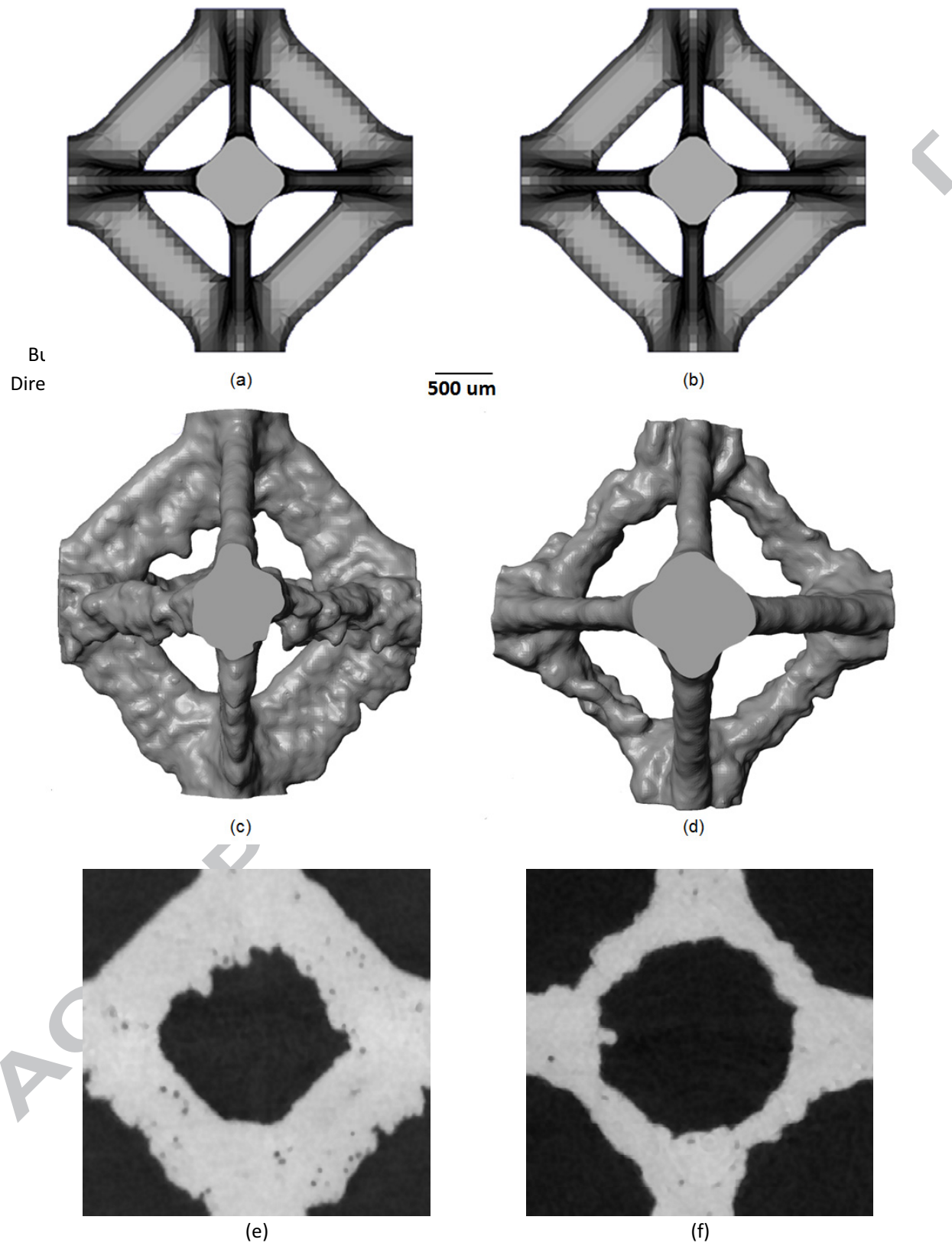


Figure 5

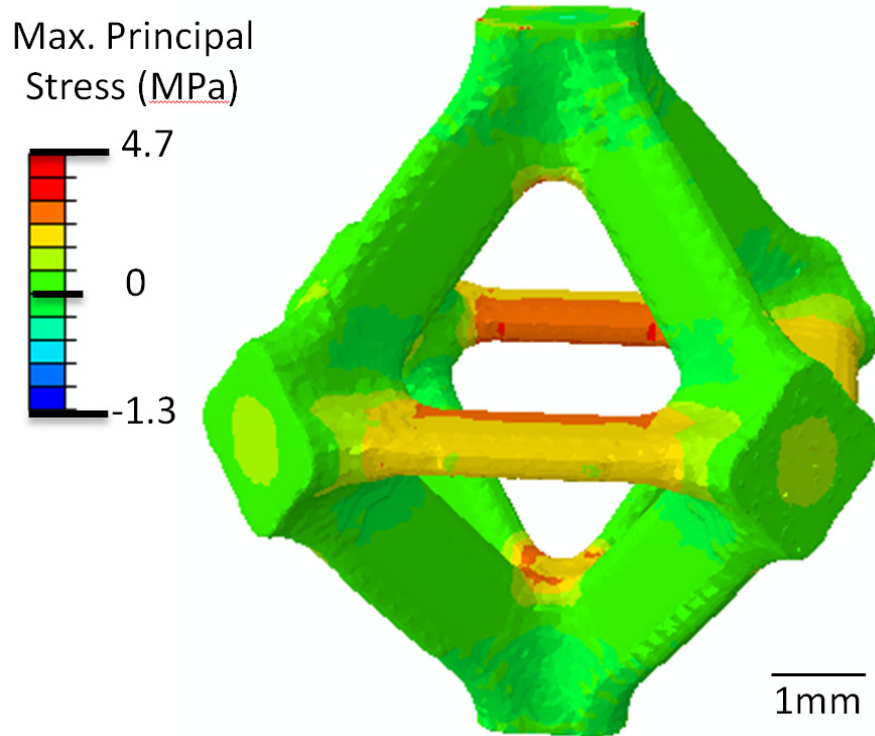


Figure 6

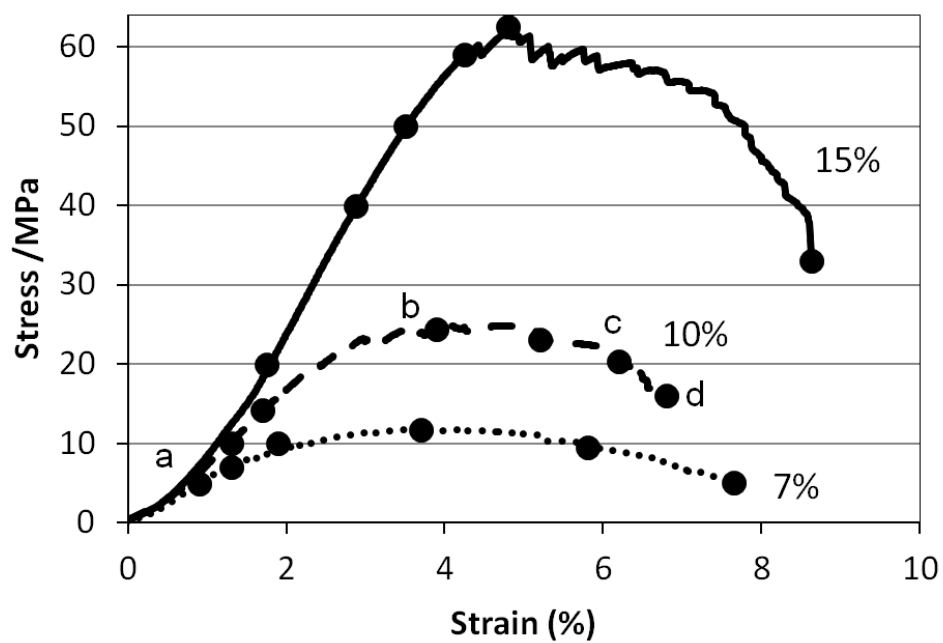


Figure 7

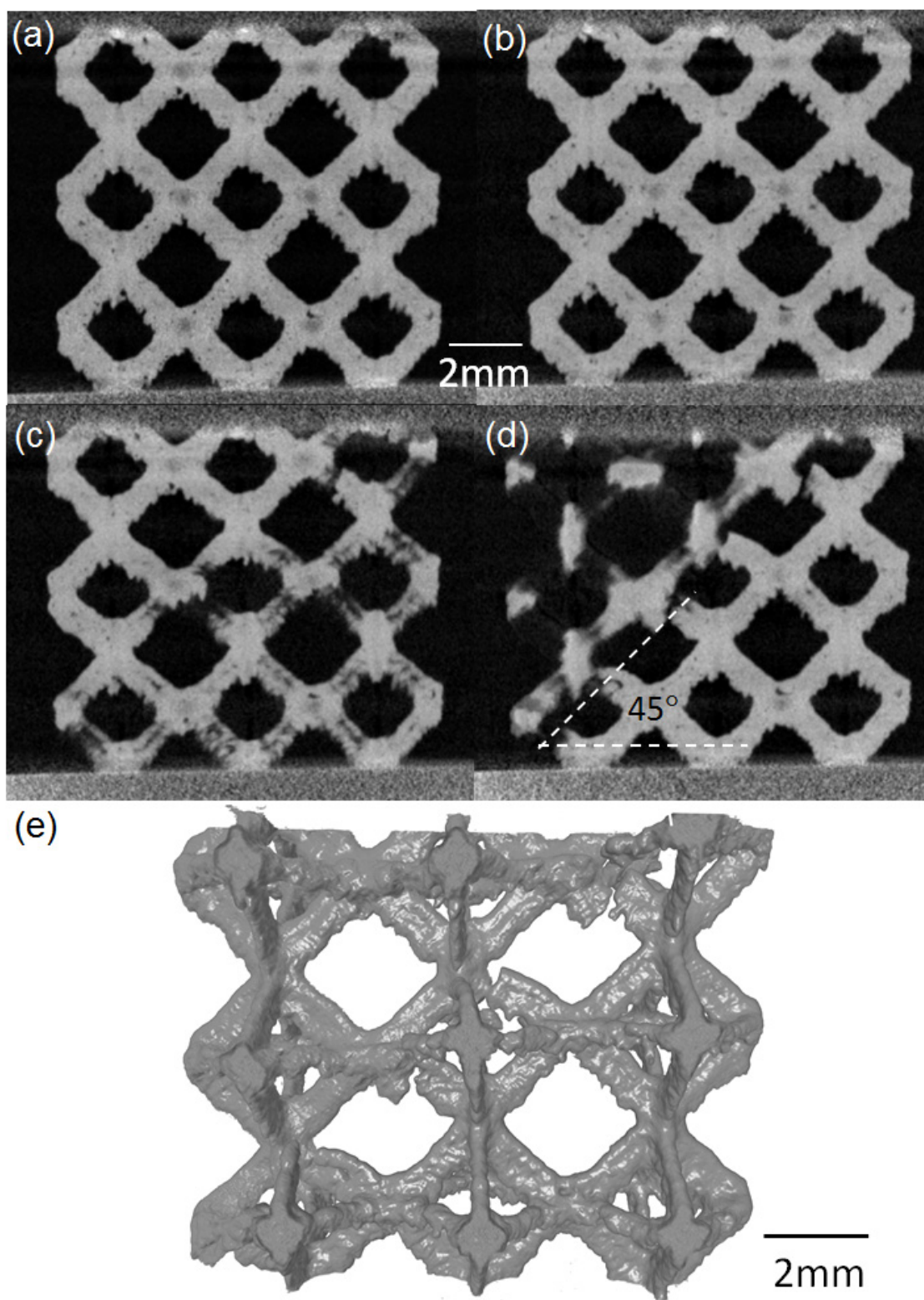


Figure 8

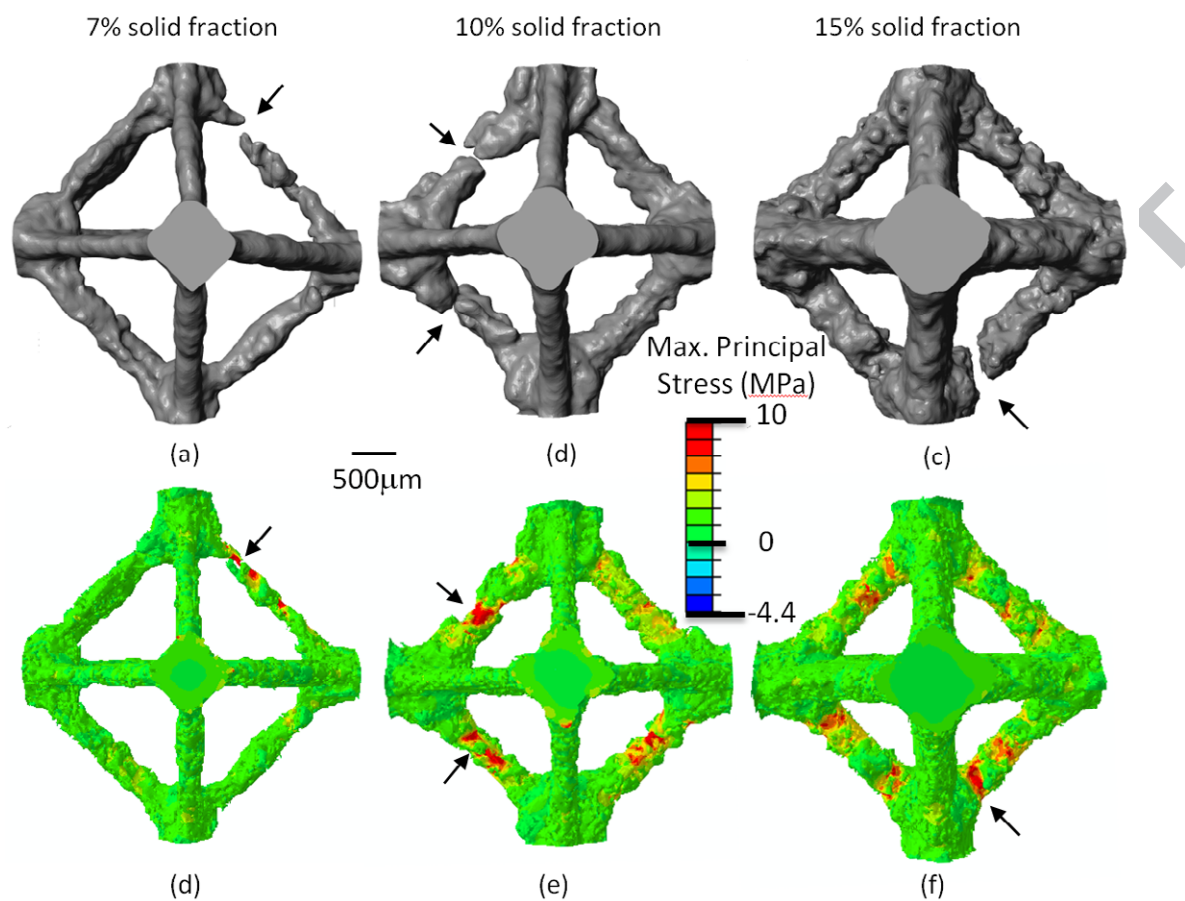


Figure 9

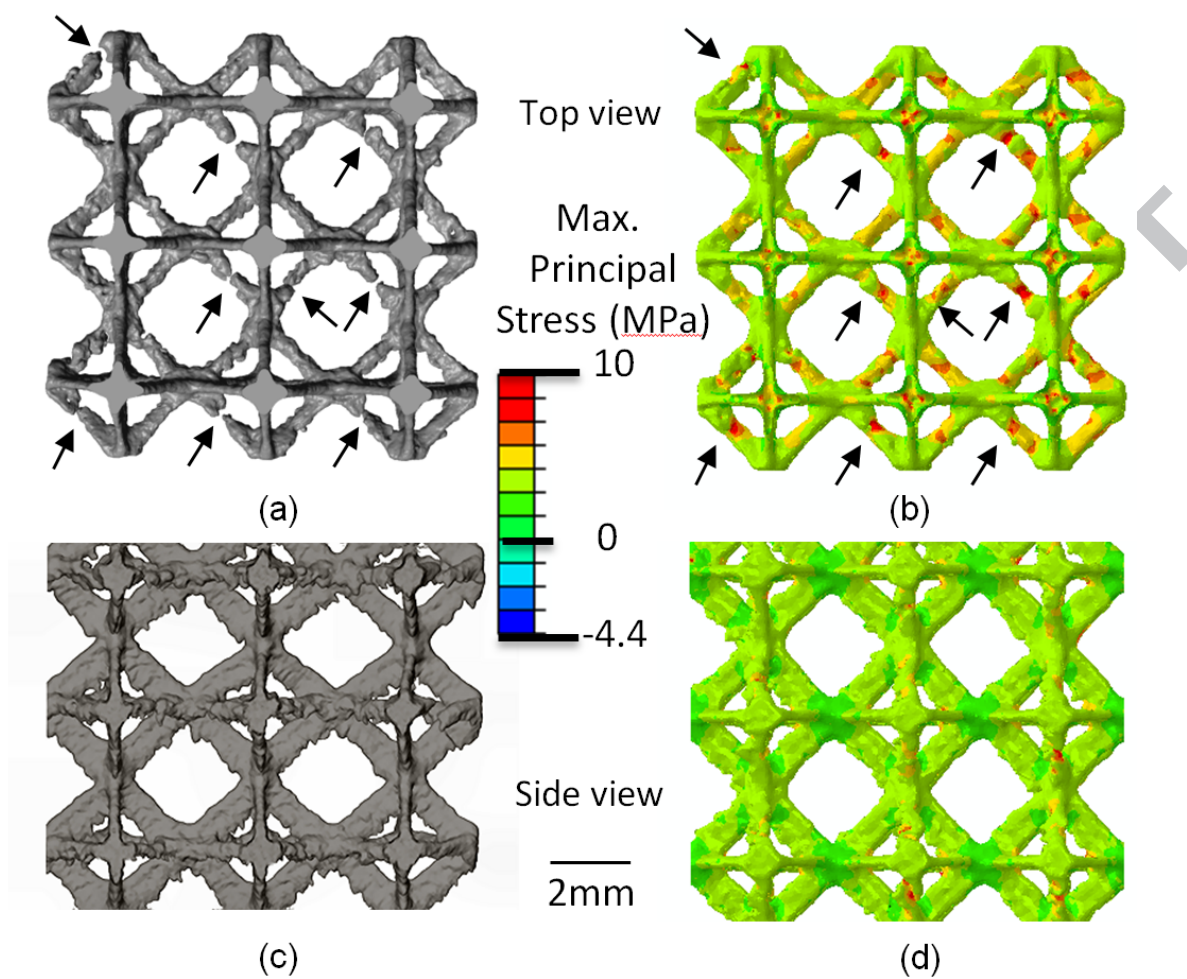


Figure 10

Table 1. Selected characteristics of the Ti-6Al-4V powder used in this work

Powder Composition (wt%)						Powder Size (μm)			Flow Rate (s/50g)	Apparent Density (%)
Ti	Al	V	O	N	Fe	d_{10}	d_{50}	d_{90}		
Bal	6.25	4.04	0.14	0.02	0.22	25.6	37.5	51.1	15.6	57.5

Table 2. Laser parameters used.

Parameter	On Powder Setting		On Solid Setting	
	Contour	Fill	Contour	Fill
Laser Power (W)	100	140	140	200
Point Distance (μm)	120	120	120	100
Exposure Time (μs)	80	80	80	80
Scan Speed (mm/s)	1500	1500	1500	1250

Table 3. Comparison between the nominal, CAD and actual as fabricated solid fraction for the scaffolds used.

Nominal solid Fraction (%)	CAD Model Solid Fraction (%)	Fabricated Solid Fraction (%)
7	6.5	7.4 ± 0.3
10	9.5	10.5 ± 0.3
15	14.7	15.4 ± 0.4

Highlights

- Selective Laser Melting was used to produce high strength scaffold structures
- In situ X-Ray Micro Tomography was used to study their failure under compression.
- Finite Element Modelling revealed that surface roughness caused high stress areas
- Failure first occurred in areas of high tensile stress predicted by the modelling
- The failure mode was very different to the classic foam materials